PNAS RESEARCH ARTICLE | BIOCHEMISTRY

Architecture of *Pseudomonas aeruginosa* glutamyl-tRNA synthetase defines a subfamily of dimeric class Ib aminoacyl-tRNA synthetases

Michael K. Fenwick[a,b,1], Stephen J. Mayclin[a,c], Steve Seibold[a,d], Amy E. DeRocher[a,b], Sandhya Subramanian[a,b], Isabelle Q. Phan[a,b], David M. Dranow[a,c], Donald D. Lorimer[a,c], Ariel B. Abramov[a], Ryan Choi[a], Stephen Nakazawa Hewitt[a], Thomas E. Edwards[a,c], James M. Bullard[e], Kevin P. Battaile[f], Iwona K. Wower[g], Aimee C. Soe[h], Susan E. Tsutakawa[h], Scott Lovell[a,d], Peter J. Myler[a,b,i,j,1], Jacek Wower[g,1], and Bart L. Staker[a,b,1]

Affiliations are included on p. 10.

Edited by Paul Schimmel, Scripps Research Florida, Jupiter, FL; received March 6, 2025; accepted April 1, 2025

The aminoacyl-tRNA synthetases (AaRSs) are an ancient family of structurally diverse enzymes that are divided into two major classes. The functionalities of most AaRSs are inextricably linked to their oligomeric states. While GluRSs were previously classified as monomers, the current investigation reveals that the form expressed in *Pseudomonas aeruginosa* is a rotationally pseudosymmetrical homodimer featuring intersubunit tRNA binding sites. Both subunits display a highly bent, "pipe strap" conformation, with the anticodon binding domain directed toward the active site. The tRNA binding sites are similar in shape to those of the monomeric GluRSs, but are formed through an approximately 180-degree rotation of the anticodon binding domains and dimerization via the anticodon and D-arm binding domains. As a result, each anticodon binding domain is poised to recognize the anticodon loop of a tRNA bound to the adjacent protomer. Additionally, the anticodon binding domain has an α-helical *C*-terminal extension containing a conserved lysine-rich consensus motif positioned near the predicted location of the acceptor arm, suggesting dual functions in tRNA recognition. The unique architecture of *Pa*GluRS broadens the structural diversity of the GluRS family, and member synthetases of all bacterial AaRS subclasses have now been identified that exhibit oligomerization.

protein translation | aminoacyl-tRNA synthetase | oligomerization

Significance

Pseudomonas aeruginosa is a common cause of hospital-related infections and a formidable health threat due to its evolving antibiotic resistance. *Pa*GluRS is homologous to other bacterial GluRSs in its domain architecture, but has evolved a distinct fold in its anticodon binding domain that introduces two interchain transfer ribonucleic acid (tRNA) binding sites through an unanticipated dimeric subunit arrangement. The structure is used to predict other members of the α2-type class Ib AaRS family, including GluRSs from pathogenic organisms such as *Acinetobacter baumannii*, *Moraxella catarrhalis*, and *Chlamydia trachomatis*, making the novel architecture an attractive molecular target.

The aminoacyl-tRNA synthetases (AaRSs) use diverse architectures to accurately pair tRNAs and amino acids for faithful translation of the genetic code (1, 2). This is achieved through an activated form of the amino acid, the aminoacyl-adenylate, which donates the aminoacyl functionality to the 2′ or 3′ hydroxyl group of tRNA (3–6). A subset of the AaRSs also catalyzes editing reactions to reverse noncognate substrate misactivation or tRNA misaminoacylation (7–12).

The AaRSs are grouped into one of two classes (I and II) based on the core fold of their catalytic domains, Rossmann or antiparallel β-sheet (13–16), respectively, which contain particular consensus sequence motifs used for binding ATP (17–21). The two classes are further partitioned into six or seven subclasses, Ia-c and IIa-c(d), based on additional sequence and structural homology (21–23). All of the AaRSs except AlaRS also contain an anticodon arm binding domain. Seven AaRSs have posttransfer editing domains (24), and the synthetases found in higher organisms commonly contain additional structural elements used for tRNA binding and multisynthetase complex formation (2).

Oligomerization is vital to the functioning of the majority of AaRSs. Nearly all of the class II synthetases form α_2 homodimers (1, 16, 19) or $(\alpha\beta)_2$ heterotetramers (25–28). A key element of these architectures is a conserved interfacial motif (motif 1) in the core fold, which was shown through mutational studies of AspRS to be essential for the catalytic function (29). Many class II synthetases have also clearly evolved ways of enhancing their interaction with tRNA leveraging oligomerization. This has been demonstrated for the class IIa enzymes, which make numerous contacts with a given tRNA substrate using both subunits (30–34). This has not been observed, however, for class IIb structures, with the tRNA-bound AspRS showing only glancing interactions involving the distal catalytic chain (35). AlaRS, a dimeric class IIa/d enzyme, binds the tRNA D-, T-, and acceptor arms through a *C*-terminal domain that is intertwined with its neighboring counterpart, which also contributes to the tRNA binding surface (36). In the case of the heterotetrameric GlyRS and PheRS synthetases, which differ structurally and belong to different subclasses, minimal catalytic subunits are employed and

Author contributions: M.K.F., T.E.E., P.J.M., and B.L.S. designed research; M.K.F., S. Seibold, A.E.D., S. Subramanian, I.Q.P., D.M.D., D.D.L., A.B.A., R.C., S.N.H., J.M.B., K.P.B., and S.L. performed research; J.M.B., I.K.W., and J.W. contributed new reagents/analytic tools; M.K.F., S.J.M., J.M.B., A.C.S., S.E.T., and S.L. analyzed data; P.J.M. procured funding; and M.K.F., A.E.D., S. Subramanian, S.L., and B.L.S. wrote the paper.

The authors declare no competing interest.

This article is a PNAS Direct Submission.

[1]To whom correspondence may be addressed. Email: Michael.Fenwick@seattlechildrens.org, Peter.Myler@seattlechildrens.org, wowerja@auburn.edu, or Bart.Staker@seattlechildrens.org.

This article contains supporting information online at https://www.pnas.org/lookup/suppl/doi:10.1073/pnas.2504757122/-/DCSupplemental.

Published May 9, 2025.

much of the tRNA recognition occurs through the noncatalytic β-subunits (37–39).

Within class I, the smaller AaRSs of subclass Ic dimerize through a conserved α-helical insertion in their catalytic domains and utilize the *C*-terminal domain of the opposite chain for anticodon arm recognition; the configuration, however, requires that the tRNA uncharacteristically engages the catalytic domain from the major groove side (13, 15, 40–44). Dimerization is less prevalent in class Ia (45–47), and the class Ib enzymes are generally considered to be monomeric outside their participation in multisynthetase complexes (2).

GluRS, a class Ib synthetase, typically adopts an extended conformation that enables interaction with the tRNA's acceptor and anticodon arms. However, its paralogs display remarkable diversity in their anticodon binding domains. Whereas bacterial and organellar GluRSs utilize α-helical subdomains (48) evolutionarily related to ones found in the class I LysRSs (49), archaebacterial and eukaryotic cytosolic GluRSs use tandem six-stranded β-barrels (50) homologous to those found in GlnRSs (51). Diversity in the anticodon binding domain also contributes to the nondiscriminating glutamylation of tRNA(Gln) within the transamidation pathway (52–55). Additionally, Glu-Q-RS, a paralog of GluRS that glutamylates queuosine at the wobble position of tRNA(Asp), lacks an anticodon binding domain (56, 57).

An unresolved anomaly in the phylogeny of the GluRS family involves the misalignment of the natural species phylogeny with that of a noncanonical subfamily of GluRSs, which includes several infectious disease targets such as *Pseudomonas aeruginosa*, *Acinetobacter baumannii*, *Moraxella catarrhalis*, and *Chlamydia trachomatis* (58). Intriguingly, the sequences of the target GluRSs are homologous to canonical GluRSs (58), including that of *Escherichia coli* GluRS, which is known to be monomeric and to display the classic elongated conformation (59). The presence of a single chromosomal *gltX* gene rules out the possibility of paralogy, and previous work showed that the *P. aeruginosa* enzyme displays the canonical biochemical activity (60), thus raising questions about the underlying structural basis of its irregular branching pattern.

Here, the structural features of *P. aeruginosa PAO1* GluRS that resolve the anomaly are elucidated using X-ray crystallography. The anticodon binding domain is demonstrated to be of the α-helical type, but has diverged from the canonical forms of GluRS in both of its subdomains. Remarkably, dimerization via symmetric intermolecular three helix bundles brings about ~180-degree rotations of much of the anticodon binding domains. Consequently, the subunits are arched rather than elongated, with the *C*-terminal domain directed back toward the active site, forming two potential intersubunit tRNA binding sites. Additionally, the *C*-terminal domain contains a novel α-helical extension rich in lysine residues situated in close proximity to the active site. Based on a conserved consensus motif within the extension, a family of *Pa*GluRS-like enzymes was identified that is expected to display similar architectures, and which includes the GluRSs of the aforementioned infectious disease targets.

Results and Discussion

α2 Oligomeric Architecture Revealed in Crystal Structure. *Pa*GluRS is the product of the *gltX* gene, which encodes 494 amino acid residues having an overall molecular weight of 56.7 kDa. Two crystal structures of an *N*-terminally tagged *Pa*GluRS construct bound to or lacking zinc were determined by molecular replacement and refined to resolutions of 2.30 and 2.45 Å, respectively (*SI Appendix*, Table S1). The crystals belong to space group $P2_12_12_1$ and the asymmetric units contain two molecules of *Pa*GluRS. For the former, 488 residues of chain A and 482 residues of chain B were built into the electron density.

Unlike the canonical GluRSs, which are monomeric, *Pa*GluRS forms a stable homodimer, as demonstrated by its crystal structure and size exclusion chromatograph. Analysis of the protein interfaces in the crystal reveals two molecules of *Pa*GluRS related by noncrystallographic twofold pseudosymmetry, with a buried surface area of 2,961.3 Å^2 (theoretical ΔG for complex dissociation of 17.4 kcal/mol) (Fig. 1*A*) (61, 62). Sizing column profiles of UV light absorbance at 280 nm and molecular weight derived from multiangle light scattering (MALS) show a major peak having a mass of 117 kDa (Fig. 2*A* and *SI Appendix*, Fig. S1). SAXS experiments confirm that the shape of the scattering species in solution is consistent with the crystal structure (χ^2 < 0.5; *SI Appendix*, Fig. S2 and Table S2), a gel shift assay demonstrates that the protein binds tRNA (*SI Appendix*, Fig. S3), and the enzymatic activity is similar to that measured for a previously published construct of *Pa*GluRS having a *C*-terminal purification sequence (60) (*SI Appendix*, Fig. S4).

The *Pa*GluRS subunits display a sequential arrangement of catalytic and anticodon binding domains like the canonical GluRSs. However, the overall subunit conformation is shaped like a horseshoe or pipe clamp, and the two subunits pack in a back-to-back arrangement with the two active sites separated by ~80 Å (Fig. 1*A*). The catalytic domain consists of a Rossmann-like core fold with an acceptor arm binding domain insertion, followed by an α-helical D-arm binding domain (domains I-III). The first conserved ATP binding motif is an "HVGT" variant that also occurs in some canonical GluRSs such as *Thermus thermophilus* GluRS, and the second motif is a common "KLSKR" variant. The acceptor arm binding domain contains a $CxCx_{24}C$ motif, commonly found in bacterial as well as eukaryotic GluRSs, that forms an α-helix and coordinates zinc using the three cysteines and a tyrosine (63–66). Catalytic domain superposition shows asymmetry, with much of domain II in chain B rotated inward by 10 degrees (Fig. 1 *B*, *Bottom*) (67).

The anticodon binding domain comprises all α-helical subdomains (domains IV and V). Domain IV is structurally homologous to the helical bundles observed in other structurally characterized GluRSs, but, as described below, exhibits an irregular folding pattern. Domain V contains the conserved α-helical cage fold commonly found in bacterial and organellar GluRSs but, strikingly, has a novel 21-residue extension at its *C*-terminus. The extension contains a 12-residue α-helix (residues 479 to 491) rich in lysine residues that is directed back toward the active site (Fig. 1 *B* and *C*).

The *Pa*GluRS homodimer is formed by interactions involving domains III and IV (Fig. 2*B*). The core of the interface contains a pair of rotationally symmetric three-helix bundles that are each assembled *intermolecularly*, with helix α12 of one chain paired with helices α13 and α14 of the other chain. The three-helix bundles interact weakly through the side chains of Leu343, Leu348, Ala366, and Phe373 (Fig. 2*C*). Additional interchain contacts are formed through the region containing helices α13 and α14 of one chain and, in the opposite chain, helix α11 and the loop connecting helices α8 and α9. The helices forming each bundle pack via hydrophobic interactions, whereas domains III and IV interact via both hydrophobic and hydrogen bonding interactions; altogether, the dimer interface contains twelve hydrogen bonds on the basis of a 3.5 Å cutoff. (Fig. 2 *C* and *D*).

Uniquely Bent Subunit Conformation. The bent subunit conformation of *Pa*GluRS contrasts remarkably with extended conformations adopted by the other structurally characterized

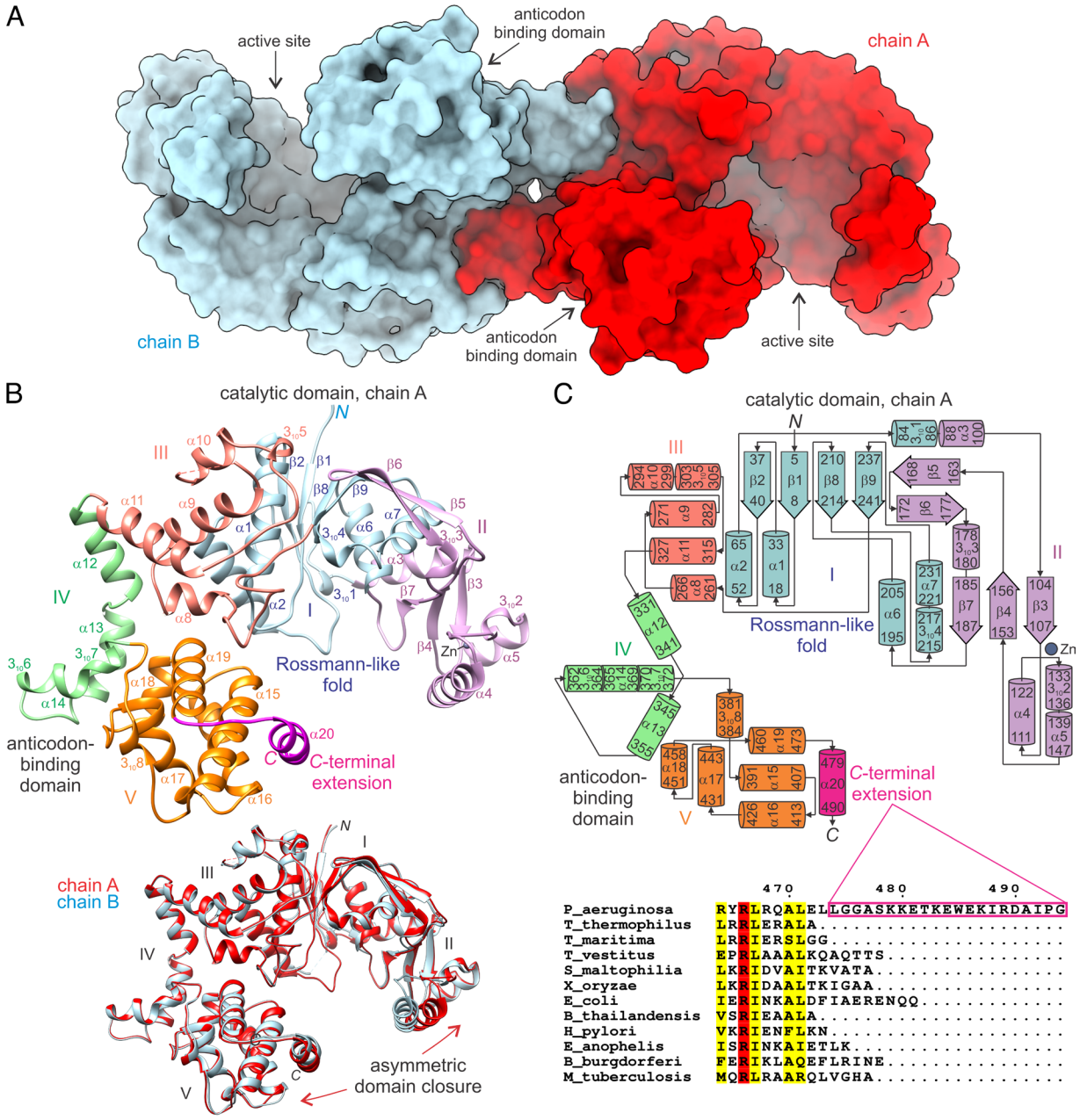

Fig. 1. Crystal structure of *Pa*GluRS. (*A*) Homodimeric architecture displaying noncrystallographic twofold pseudosymmetry. (*B*) Subunit architecture. Chain A of the asymmetric unit is shown in ribbon representation with secondary structural elements labeled. The catalytic and anticodon binding domains comprise subdomains I-III and IV-V, respectively. Domain V contains a twenty-one residue *C*-terminal extension. At the *Bottom*, the subunits are superimposed to highlight the asymmetry. (*C*) Secondary structural topology, with β-strands depicted as thick arrows and α- and 3_{10} helices as cylinders. Below, the amino acid sequence of the *C*-terminal extension is aligned with other PDB entries (Fig. 3*A*), with aligned sites showing absolute conservation and similarity near the *C* termini colored red and yellow, respectively.

bacterial GluRSs (Fig. 3 *A*, *Left*). The closest structural ortholog is *T. thermophilus* GluRS (*Tt*GluRS, PDB code 2CV1), which has a DALI Z-score of 42.2, corresponding to the alignment of the catalytic domains (68). However, the structures also overlay closely when alignments are performed instead based on the anticodon recognition domains, through helix α13 (Fig. 3 *A*, *Right*).

With the catalytic domains overlayed, the anticodon recognition domains of *Pa*GluRS and *Tt*GluRS are related by a screw-like displacement with a rotation and translation of 177.9° and −4.5 Å, respectively (67) (Fig. 3*B*). The bending region maps to the residues connecting the first and second helices (α12 and α13) of the intermolecular three-helix bundles of *Pa*GluRS, which recapitulate the *intramolecular* three-helix bundle of *Tt*GluRS. In the canonical GluRSs, this region contains amino acid insertions of various lengths (Fig. 3*C*) and is structurally diverse. Leu343 of chain A and Asn344 of chain B of *Pa*GluRS, which span the canonical insertions, are separated by 10.5 Å. Thus, the unique folding pattern of the bending region of *Pa*GluRS, which enables the formation of the symmetric helical bundles within the dimer, is one of the distinguishing features of the noncanonical architecture.

The subunit conformation of *Pa*GluRS is stabilized through a complex array of nonbonded interactions near the bending region and meeting point of domains III-V, including the adjacent chain (Fig. 3*D*). The side chain of Trp341, the central residue of the bending region and last residue of helix α12, is stabilized via hydrogen bonding with the backbone of Arg266 of domain III. Interestingly, α-helical backbone hydrogen bonding is prevented

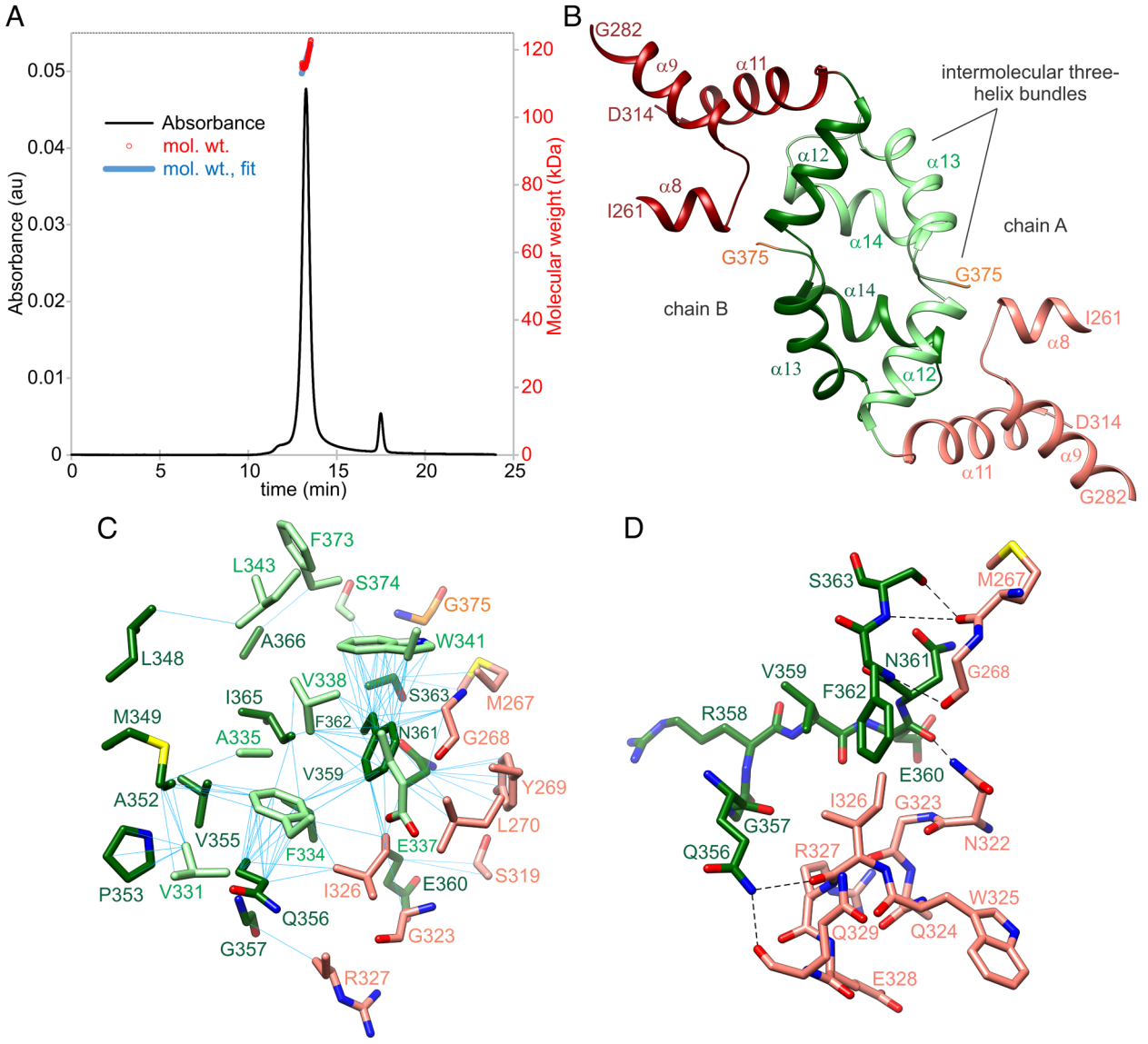

Fig. 2. Evidence for dimerization of *Pa*GluRS. (*A*) Dimer formation in solution. Size exclusion chromatogram is shown with UV absorbance trace at 280 nm (primary axis) and MALS-derived molecular weight (secondary axis). (*B*) Dimer interface architecture. Symmetric 3-helix bundles formed by domain IV comprise the interface core and interact with domain III. (*C*) Hydrophobic interactions. Close contacts between carbon atoms of hydrophobic groups in half the interface (separation distances ≤ 4.7 Å) are indicated with blue lines. (*D*) Hydrogen bonding interactions. Six potential hydrogen bonds in half the interface are shown as dashed lines. In panels (*B*–*D*) chain B residues are colored using darker tones.

by the presence of Pro345. Trp341 adopts a t90°-like rotamer (74) with the indole moiety packed closely against the methyl group of Ala342, an insertion, and wedged between the side chains of Phe373 of the same subunit and Phe362 of the opposite chain. The reach of the indole moiety appears to provide enough of a platform for Phe373 stacking, allowing its interaction with Tyr347. In this conformation, the Tyr347 hydroxyl group can hydrogen bond with the guanidinium of Arg266, which, in turn, is ideally oriented to form two additional hydrogen bonds with the backbone of Leu458 of domain V. Within the kink separating helices α12 and α13, Asn344 forms helix-bridging hydrogen bonds via its side chain with the backbone carbonyl oxygen of Gln339 and the amide nitrogen of Tyr347. Additionally, backbone–backbone hydrogen bonding occurs between the amide nitrogen of Leu343 and the carbonyl oxygen of Val338.

Intersubunit tRNA Binding Sites Identifiable in Dimer. The genome of *P. aeruginosa* PAO1 contains open reading frames encoding both *Pa*GluRS and *Pa*GlnRS, obviating the need to produce Gln-tRNA(Gln) via a mischarged Glu-tRNA(Gln) (75). tRNA(Glu) plays a cofactor role in aminoacyl-adenylate intermediate formation, common to class Ib synthetases and ArgRS (60, 76–80). Although tRNA(Glu) may have CUC and UUC anticodons in general, the *P. aeruginosa* genome encodes only a single tRNA(Glu; $U_{34}U_{35}C_{36}$) isotype (81) (tRNA numbering according to ref. 82).

Novel modes of recognition of one or two tRNAs by *Pa*GluRS may be readily predicted based on superpositions with high-resolution crystal structures of *Tt*tRNA(Glu;CUC)-bound *Tt*GluRS (55, 73, 83). Notably, the location of the anticodon binding domain in the conformation of *Pa*GluRS prohibits its binding to the anticodon of a tRNA having its acceptor arm bound at the active site of the same subunit (Fig. 4*A*). This contrasts with complexes formed by *Tt*GluRS in which the tRNA interacts with all five domains (Fig. 4*B*). However, through the ~180-degree rotation of the anticodon binding domain and dimerization, each catalytic domain of *Pa*GluRS, together with the anticodon binding domain of the twofold related chain, forms an intersubunit tRNA binding site similar in shape to the one formed by the extended

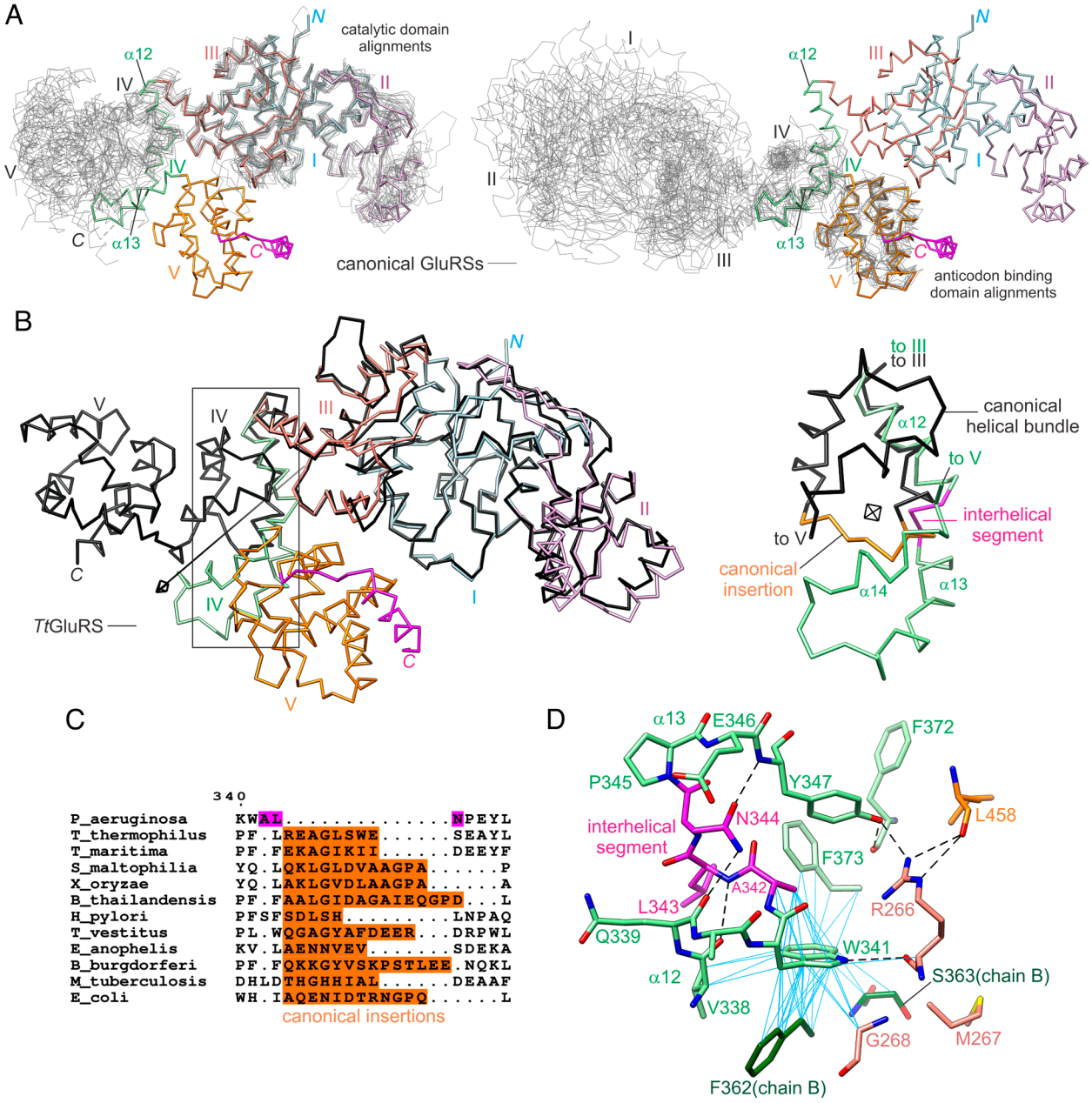

Fig. 3. Noncanonical subunit conformation of *Pa*GluRS. (*A*) The catalytic domain and much of the anticodon binding domain (sticks) align closely with the corresponding domains of other bacterial GluRSs (gray wires). Shown are *Cα* atom superpositions of GluRSs of the following organisms onto domains I-IV (*Left*) and domains IV-V (*Right*) of *Pa*GluRS: *Thermosynechococcus vestitus*, *Thermotoga maritima*, *Mycobacterium tuberculosis*, *Burkholderia thailandensis*, *Xanthomonas oryzae*, *Borrelia burgdorferi*, *Helicobacter pylori*, *Elizabethkingia anophelis*, *Stenotrophomonas maltophilia, T. thermophilus*, and *E. coli* [PDB entries 2CFO (69), 2O5R, 2JA2, 4G6Z (65), 5H4V (70), 4GRI (65), 6B1P (71), 6B1Z (72), 7K86, and 1N78 (73), 8I9I (59), respectively]. (*B*) *Cα* atom traces of *Pa*GluRS and *Tt*GluRS aligned in reference with a screw axis that relates the anticodon binding domains (67). *Inset*: Close-up view of domain IV. (*C*) Insertions (manually aligned structurally, orange) near the bending region in other structurally characterized bacterial GluRSs. (*D*) Nonbonded interactions. Potential hydrogen bonds are shown as dashed lines and hydrophobic contacts involving Trp341 as blue lines.

conformation of *Tt*GluRS (Fig. 4 *B* and *C*). Remarkably, the conformational change in helix α13 relative to α12 and the amino acid insertions in *Tt*GluRS (Fig. 3*B*) result in an overlapping of the helical bundles with the consequence of conserving the spatial disposition (via the dimer in *Pa*GluRS) of Arg358, the C36 binding residue (Fig. 4*D*).

The placement of the *C*-terminal α-helix also suggests a function of acceptor arm recognition through the anticodon binding domain (Fig. 4*E*). The helix contains four lysine residues (Lys479, Lys480, Lys483, and Lys487), shown below to be conserved, having disordered side chains lacking any interaction with the protein. Three are directed into the opening of the active site. After subdomain V is rigidly overlayed onto tRNA-bound *Tt*GluRS (which was first superimposed onto a *Pa*GluRS catalytic domain within the dimer) to recognize the anticodon loop, the *C*-terminal helix resides within closer reach of the acceptor arm, although the nature of the interaction cannot be predicted based on this simple representation (*SI Appendix*, Fig. S5). (That Lys480 is oriented away from the active site suggests that a significant structural change must take place.) Whether the helix can disengage from domain V is also unclear, and the presence of two conserved glycine residues in the loop preceding the helix is intriguing. Despite this, the structure shows that the helix can pack tightly against domain V electrostatically via residues at its *N*- and *C*-terminal ends and via hydrophobic contacts formed through its *C*-terminal amphipathic face.

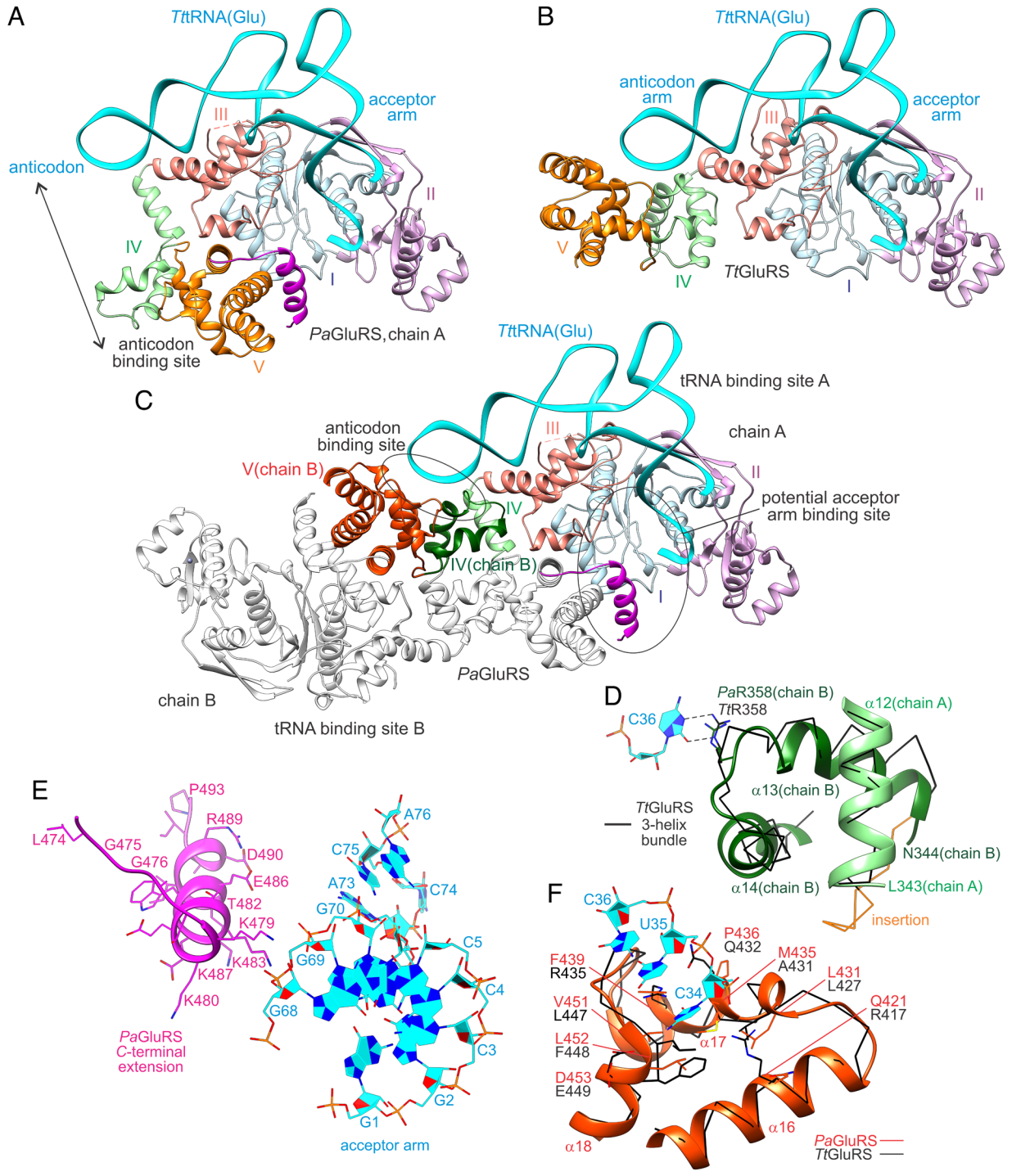

Fig. 4. Hypothetical modes of tRNA recognition by *Pa*GluRS. tRNAs were placed via superpositions with unmodified *Ttt*RNA(Glu; CUC)-bound *Tt*GluRS [PDB entry 1N78 (73)]. (*A*) Inability of anticodon binding domain of *Pa*GluRS to bind anticodon of tRNA bound to the catalytic domain of the same subunit. (*B*) tRNA recognition by all five domains of *Tt*GluRS. (*C*) Formation of two potential intersubunit tRNA binding sites by *Pa*GluRS dimer, with *C*-terminal extension serving as additional acceptor arm recognition site. Domains forming one tRNA binding site are colored to highlight canonical-like substructure. (*D*) Spatial conservation of Arg358 through dimer formation. (*E*) *C*-terminal extension and its disposition near the acceptor arm. Disordered side chains are modeled based on their high-probability rotamers. (*F*) Potential anticodon recognition site formed by domain V.

The structure of the putative anticodon binding site in domain V is similar to that of *Tt*GluRS in secondary structure, but shows considerable differences in amino acid usage (Fig. 4*F*). A shallow cleft is formed by 3 helices (α16-α18), and several hydrophobic residues (Leu431, Met435, Val451, and Leu452, which align with Leu427, Ala431, Leu447, and Phe448, respectively, of *Tt*GluRS) form the base of the putative U34 binding site. Phe439, which is positioned near U35, replaces a highly conserved arginine residue that stacks against the uracil moiety of U35 and forms a hydrogen bond with the cytosine moiety of C34 of *Ttt*RNA(Glu;CUC) (55). Other residues having notable spatial locations within the anticodon binding site include Arg432 and Lys413.

Conserved Signature Sequences Suggest a Structurally Homologous GluRS Subfamily. The amino acid sequence of the *Pa*GluRS *C*-terminal extension was used to search databases of bacterial GluRSs for orthologs closely related to *Pa*GluRS (*Materials and Methods*). These proteins are found across *Chlamydiia*, which interestingly, in

the context of tRNA recognition, lack a glutaminyl-tRNA synthetase and specific tRNA modification enzymes, including the wobble base modification biosynthetic enzyme MnmCD. Numerous putative noncanonical orthologs are also found in γ-*proteobacteria*, and a smaller number exist in α- and δ-*proteobacteria*, *Holophagae*, and "*Candidatus* Uabimicrobiia" (Fig. 5*A*). Notable bacterial pathogens among these various classes include *A. baumannii*, *M. catarrhalis*, *C. trachomatis,* and *Chlamydia pneumoniae*. A multiple sequence alignment of the noncanonical GluRSs shows a conserved consensus motif, LGGΦSKKxxKxΦEK, within the *C*-terminal extension, where Φ and x denote hydrophobic residues and lack of conservation, respectively (Fig. 5*C* and *SI Appendix*, Fig. S6). The motif maps to the first nine residues of the *C*-terminal α-helix and the preceding loop (Fig. 5*B*).

The multiple sequence alignment of the noncanonical bacterial GluRSs reveals several additional conserved sequence sites that appear to be strongly conserved in this family of enzymes. One such site in the catalytic domain is *Pa*Asp15, located near the first ATP binding motif (Fig. 6*A*). In the structure, its carboxylate forms an interdomain salt bridge with Arg464 of domain V, which is also significantly conserved (Fig. 6*B*). In the canonical GluRSs, the corresponding sites are separated by ~50 Å. An additional highly conserved site is *Pa*Gln184, located near the binding site of tRNA A76.

Within domain IV, *Pa*Trp341 is the most strongly conserved residue among those unique to the noncanonical subset (Fig. 6*A* and *SI Appendix*, Fig. S6). Asn344 is not absolutely conserved but is utilized by the majority of these enzymes. Interestingly, the number of amino acid residues corresponding to the three helical segments of domain IV is nearly constant (Fig. 6*A*).

Within domain V, in addition to the *Pa*GluRS Arg464 site noted above, *Pa*Gln399, Leu402, Trp403, and Glu406, all show a high degree of sequence conservation (Fig. 6*A*). Structurally, these residues compose a supporting substructure beneath the *C*-terminal extension. Glu406 forms an interhelical salt bridge with Arg468, which is conserved in the aligned α-, γ-, and δ-proteobacterial orthologs (Fig. 6*B* and *SI Appendix*, Fig. S6). The side chain of Trp403 is inserted between helix α15 and the *C*-terminal α-helix, where it packs with several domain V residues, including the highly conserved Gln399. Conservation also includes sites on the opposite side of the domain V, namely *Pa*Lys413, Arg432, and Phe439, which reside within the putative anticodon binding site (Fig. 6*C*). In most species of *Chlamydiia*, Phe439 is replaced with a tyrosine, which is also observed in the class I LysRSs (49). Collectively, the presence of highly conserved residues on the two sides of domain V (including the *C*-terminal extension) poised to bind the acceptor and anticodon arms of tRNA strongly supports a dual functioning in tRNA recognition.

Concluding Remarks. For the majority of AaRSs, oligomerization constitutes an essential component of the tRNA recognition framework. The prokaryotic class Ib enzymes are typically larger than the class Ic enzymes and are classified as monomers (2) having extended chain conformations that enable interaction with both the acceptor and anticodon arms of tRNA (18, 48, 49). Thus, the unusual dimeric architecture displayed by *Pa*GluRS, which represents a novel family of α2 class Ib AaRSs, is especially noteworthy given the homology of its five subdomains with those of canonical GluRSs such as *Tt*GluRS. While the dimer interestingly is formed through a packing of helical bundles similar to dimer formation in class Ic synthetases (15, 40), domain IV instead functions as the core dimerization module, and the catalytic domain is predicted to bind the minor groove of the acceptor arm of tRNA.

The distinguishing features of the *Pa*GluRS fold relative to other GluRSs are its use of intermolecular helical bundles and a *C*-terminal extension placed near the active site through an arched subunit conformation. The rotation of helix α13 within the symmetrical packing of domain IV of the two chains maintains the spatial location of Arg358, which is known to bind nucleotide 36 in monomeric GluRSs (55). The canonical fold of domain IV typically positions this residue via an intramolecular three-helix bundle. However, as noted in Fig. 3, there is a variable region between the first two helices that in other bacteria [e.g., *Gloeobacter violaceus* (84)] is expanded considerably. The lack of a *C*-terminal extension in the GluRSs of deeply branching extant bacteria, including the canonical *Thermotoga maritima* GluRS (PDB entry 2O5R), which has an α-helical cage domain that branches more closely to the class I LysRSs (*SI Appendix*, Fig. S8), suggests that the *Pa*GluRS architecture represents an adaptation that enhances interaction with tRNA.

Consideration of a hypothetical extended conformation of *Pa*GluRS introduces two apparent structural anomalies. First, an overlay of domain V onto the extended conformation places the conserved *C*-terminal helix at the very back of the enzyme, at a considerable distance from the anticodon arm (*SI Appendix*, Fig. S7 *A* and *B*). Because Arg358 in domain IV is placed at its canonical location via the dimerization, the tRNA likely adopts the canonical binding arrangement in that region. The *C*-terminal helix would not be expected then to wrap around domain V to bind the anticodon arm. Such a disposition would only further obscure the unknown function of the helix and motif, which might otherwise be presumed to be one of acceptor arm binding based on its positioning near the catalytic domain. This also follows from the known tRNA binding functions of *N*-terminal helical extensions in Eukaryotic class IIb AaRSs having similar motifs (85, 86).

Second, superpositioning helices α12 and α13 onto the extended conformation of *Tt*GluRS reveals a gap of 10 Å between residues 343 and 344 related to the absence of the insertions observed in the canonical GluRSs (*SI Appendix*, Fig. S7 *A* and *B*). Interestingly, a template-based solution that forces adoption of the extended conformation recapitulates the structure through a shortening of helix α12 and burial of Trp341 (*SI Appendix*, Fig. S7*C*). While this fold may be feasible in principle, we have not yet identified conditions that yield such a conformation. What is unlikely, however, is the persistence in solution of the monomeric, bent conformation (Fig. 4*A*), as numerous hydrophobic residues in helices α12-α14 would be exposed to the solvent.

The crystal structure of *Pa*GluRS was determined through structural genomics efforts at the Seattle Structural Genomics Center for Infectious Disease to facilitate structure-guided drug discovery (87–89). The essential role AaRSs play in protein translation (90, 91) establishes the two classes of synthetases as promising drug targets, and structural differences between the PaGluRS-type synthetases of pathogenic bacteria and their human cytosolic and mitochondrial homologs may be considered for achieving target selectivity.

Materials and Methods

Protein Expression, Purification, and Analysis. Cloning, expression, and purification followed standard protocols previously described (92, 93). The full-length GluRS gene from *P. aeruginosa* (UniProt accession ID Q9XCL6) encoding amino acids 1 to 494 was PCR-amplified from genomic DNA using forward primer 5′-CTCACCACCACCACCACCATATGACCACTGTTCGTACTCGCAT-3′ and reverse primer 5′-ATCCTATCTTACTCACTTAGCCGGGAATGGCGTCGCGG-3′. The gene was cloned

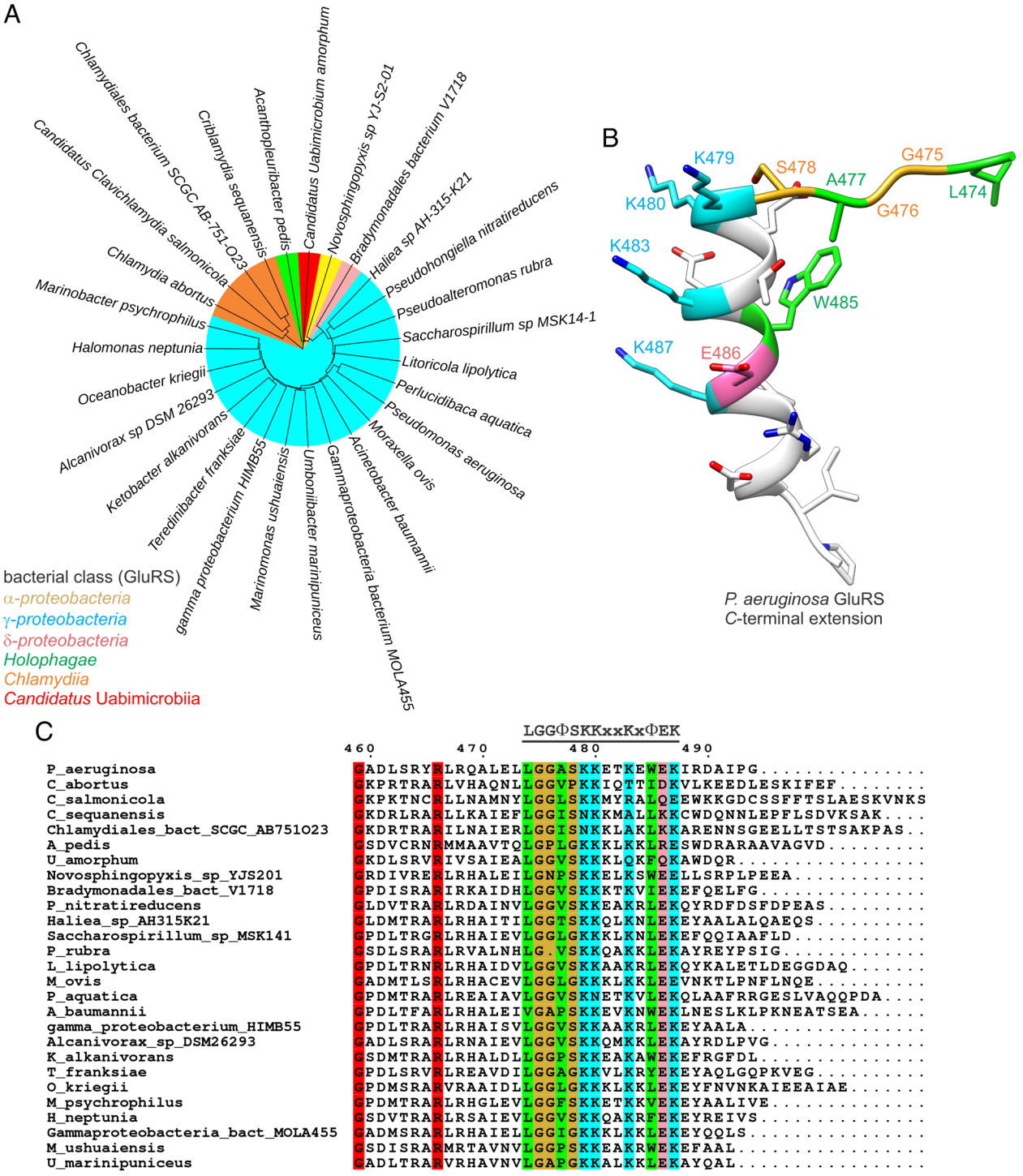

Fig. 5. Noncanonical GluRSs and their *C*-terminal extensions. (*A*) Bacteria possessing a putative noncanonical GluRS represented using a phylogenetic tree based on amino acid sequences, with branches colored by class. (*B*) Mapping of conserved amino acid residue sites in *C*-terminal extensions onto the structure of *Pa*GluRS. Sites having consensus hydrophobic, basic, and acidic residues are colored green, cyan, and pink, respectively. Sites rich in glycines or serines are colored goldenrod. (*C*) Consensus motif from multiple sequence alignment of GluRSs in panel (*A*). Conserved sites within the motif are colored according to panel (*B*) whereas proximal sites outside the motif showing absolute conservation are colored red.

into the ligation-independent cloning (LIC) vector pBG1861 encoding a noncleavable hexahistidine tag (MAHHHHHH-ORF) (93, 94), and chemically competent *E. coli* BL21(DE3)-R3-pRARE2 cells were transformed with the plasmid (95). The hexahistidine tagged *Pa*GluRS was expression-tested, and 2 L of culture were grown using autoinduction media (96) in a LEX Bioreactor (Epiphyte Three Inc.). The expression clone PsaeA.01348.a.B1.GE38278 is available at https://www.ssgcid.org/available-materials/expression-clones/.

*Pa*GluRS was purified in a two-step protocol consisting of an immobilized metal (Ni^{2+}) affinity chromatography (IMAC) step and size-exclusion chromatography (SEC). All chromatography runs were performed on an ÄKTA Purifier 10 (GE Healthcare) using automated IMAC and SEC programs (92). Thawed bacterial pellets (~25 g) were lysed by sonication in 200 mL buffer containing 25 mM HEPES, pH 7.0, 500 mM NaCl, 5% glycerol, 0.5% CHAPS, 30 mM imidazole, 10 mM $MgCl_2$, 1 mM TCEP, 250 μg/mL AEBSF, and 0.025% sodium azide. After sonication, the crude lysate was supplemented with 20 μL of Benzonase (25 units/μL) and incubated while mixing at room temperature for 45 min. The lysate was clarified by centrifugation at 10,000 rev min^{-1} for 1 h using a Sorvall centrifuge (Thermo Scientific). The clarified supernatant was then passed over a Ni-NTA His-Trap FF

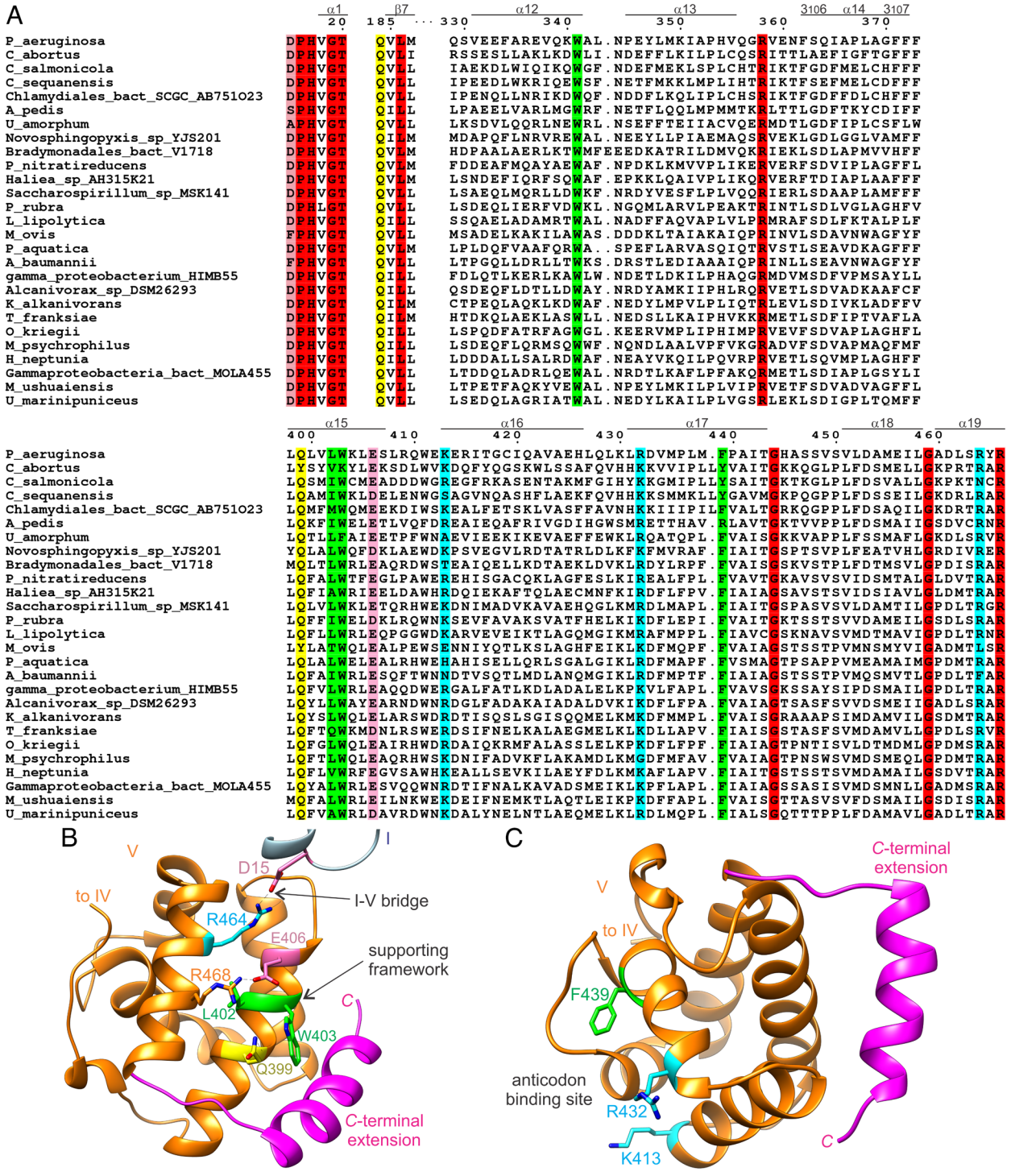

Fig. 6. Additional signature sequence sites in noncanonical GluRSs. (*A*) Multiple sequence alignment, with conserved hydrophobic, basic, acidic, and polar and neutral sites colored green, cyan, pink, and yellow, respectively. (*B* and *C*) Conserved sites in domain V near the *C*-terminal extension and catalytic domain (*B*) and within the putative anticodon binding site (*C*), colored according to panel (*A*). Potential hydrogen and ionic bonds are shown as dashed lines.

5 mL column (GE Healthcare) which was pre-equilibrated with loading buffer composed of 25 mM HEPES, pH 7.0, 500 mM NaCl, 5% glycerol, 30 mM imidazole, 1 mM TCEP, and 0.025% sodium azide. The column was washed with 20 column volumes of loading buffer and was eluted with loading buffer plus 250 mM imidazole in a linear gradient over seven column volumes. Peak fractions were pooled and concentrated to 5 mL. SEC was then performed on a column (HiLoad 26/600 Superdex 75, GE Healthcare) that was equilibrated with running buffer composed of 25 mM HEPES, pH 7.0, 500 mM NaCl, 5% glycerol, 2 mM DTT, and 0.025% sodium azide. The peak fractions were collected, analyzed via SDS-PAGE, and concentrated to 48.2 mg/mL using an Amicon purification system (Millipore). Aliquots of 110 μL were flash-frozen in liquid nitrogen and stored at −80 °C.

The first indication of oligomerization in solution was obtained via analytical SEC using the zinc-free protein (*SI Appendix*, Fig. S1). A Superdex 200 Increase 10/300 GL column (Cytiva) was equilibrated in SEC buffer (20 mM HEPES, pH 7.0, 300 mM NaCl, 5% glycerol, and 1 mM TCEP). One hundred microliters of purified protein was injected onto the column, and the UV absorbance of the column eluate was monitored at 280 nm, with 0.5 mL fractions collected. Column sizing was evaluated by comparing the retention times of size standards–beta amylase (200 kDa), bovine serum albumin (66 kDa), carbonic anhydrase (29 kDa), and cytochrome C (12.4 kDa)–with the retention time of *Pa*GluRS.

Determination of the absolute molecular weight of a zinc-treated sample was also determined with SEC-MALS at the SIBYLS beamline 12.3.1 of the Advanced

Light Source (ALS) (97). Zinc was added through a 7.5× dilution of the protein with zinc reconstitution buffer (20 mM HEPES, 150 mM NaCl, 5 mM $MgCl_2$, pH 6.5, supplemented with 0.5 mM $ZnSO_4$ and 10 mM TCEP). The sample was then diluted twofold with MALS running buffer (20 mM HEPES, 150 mM NaCl, 5 mM $MgCl_2$, pH 7.5, supplemented with 1 mM TCEP) to bring the protein to approximately 3.5 mg/mL, flash frozen in liquid nitrogen, and shipped on dry ice to the beamline. There, the sample was thawed and injected into a Shodex SEC column equilibrated with the MALS buffer and operated at a flow rate of 0.65 mL min^{-1}. The column was connected to an Agilent 1260 Infinity HPLC system. MALS was measured using an 18-angle DAWN HELEOS II light scattering detector connected with an Optilab refractive index concentration detector (Wyatt). A 55 μL sample of 7 mg/mL BSA monomer in MALS buffer, and a refractive index increment (d*n*/d*c*) value of 0.16, was used for system calibration.

SAXS analysis of *Pa*GluRS was also conducted on the outlet stream from the SEC column (*SI Appendix*, Table S2). X-ray images were recorded continuously on a Pilatus 3 2 M detector placed 2.1 m from the flow cell. The X-rays had a wavelength of 1.127 Å. Each frame corresponded to a 2 s exposure, and 660 intensity profiles were provided by the beamline for a q range of 0.0109 to 0.4729 $Å^{-1}$. The LC analysis tool in Bioxtas-raw (98) was used to obtained base line corrected profiles. An all-atom structural model based on the crystal structure of *Pa*GluRS bound to zinc, with missing atoms added using ChimeraX and MODELLER (61, 99), was fitted to the experimental curve using FoxS (100). A profile of maximum size was computed with background and offset corrections. Electron pair distance distribution functions were determined by means of the DENSS inverse Fourier transform method implemented in Bioxtas-raw (98, 101). Molecular weights based on the SAXS data were estimated using the volume of correlation (V_C) and Bayesian inference methods (102, 103).

Protein Crystallization and Structure Determination. All *Pa*GluRS crystallization experiments were carried out via sitting drop vapor diffusion at 17 °C. The enzyme was initially crystallized in its zinc-free state and more recently bound to zinc. Purified *Pa*GluRS lacking zinc (48.2 mg/mL), supplemented with 2 mM of compound BT_04B09, a *Pa*GluRS inhibitor (60), was crystallized in 96-well format in XJR compact junior plates with sample drops formed in a 1:1 ratio (0.2 μL protein, 0.2 μL reservoir solution) against 80 μL reservoir solution. The crystallant originated from the JCSG+ screen, formulation D9 (170 mM ammonium sulfate, 25.5% polyethylene glycol 4000, and 15% glycerol). Crystals were cryocooled directly via plunging into liquid nitrogen.

For zinc site reconstitution, approximately 170 μL of thawed protein was combined with 2 μL of 1 M TCEP and 8 μL of 50 mM zinc sulfate, centrifuged, incubated for approximately 18.5 h at 4 °C, and flash frozen in liquid nitrogen. The thawed protein (46 mg/mL) was supplemented with 2.5 mM adenosine-5′-sulfamate, 7.5 mM L-glutamate, and 7.5 mM $MgCl_2$ and crystallized using UVXPO MRC (Molecular Dimensions) sitting drop vapor diffusion plates and Berkeley screen (104) (Rigaku Reagents) condition D8 [20% (w/v) PEG 3350, 100 mM MES/sodium hydroxide, pH 5.5, 100 mM ammonium citrate dibasic, and 5% (v/v) 2-propanol]. Drops formed from 0.1 μL of protein and 0.1 μL crystallization solution were dispensed and equilibrated against 50 μL of the latter. Crystals were then cryoprotected by layering 2 μL of 80% (v/v) reservoir and 20% (v/v) ethylene glycol.

X-ray diffraction data were collected at APS beamline 21-ID-F and NSLS2 beamline 19-ID, respectively, where they were irradiated using X-rays having wavelengths of 0.97872 and 0.97950 Å. Reflections were integrated and scaled using XDS (105) via AUTOPROC (106). Initial phases for the zinc-free structure were determined by molecular replacement using Phaser (107) with the crystal structure of *Borrelia burgdorferi* GluRS [PDB entry 4GRI (65)] as a search model. Manual model building, automated structural refinement, and model validation were performed using Coot (108), PHENIX (109), and MolProbity (110), respectively. None of the added ligands (BT_04B09 or adenosine-5′-sulfamate, L-glutamate, and $MgCl_2$) were observed in electron density maps. Details related to the X-ray diffraction and structural refinement statistics are listed in *SI Appendix*, Table S1. Structural superpositions were carried out and molecular illustrations were prepared using Chimera and ChimeraX (61, 111, 112). Domain motions were characterized with the aid of DynDom (67). The template model was generated with SWISS MODEL (113).

Sequence Analysis. Amino acid sequence alignments were performed using MUSCLE (114), adjusted based on structural alignments, and illustrated using ESPript 3 (115). Amino acid sequences of noncanonical bacterial GluRSs were initially identified using the Aminoacyl-tRNA Synthetase Data Bank (AARSDB; Release 2021_04) (116). Sequences of bacterial GluRSs from NCBI were then individually aligned with the initial set of sequences, and additional noncanonical orthologs were identified using an ad hoc scoring function based on amino acid usage within the *C*-terminal extension. The resulting set of sequences were clustered using USEARCH (117) with a cutoff sequence identity of 66% and centroid sequences were illustrated, for convenience of presentation, as a UPGMA phylogenetic tree using MUSCLE (114) and iTol (118).

Data, Materials, and Software Availability. Three-dimensional coordinates of *Pa*GluRS are available at the PDB (https://www.rcsb.org/) under accession codes 5TGT (119) and 8VC5 (120). Accompanying SAXS data can be retrieved from Simple Scattering (https://simplescattering.com/) under accession code XSBHEVPH (121).

ACKNOWLEDGMENTS. I.K.W. and J.W. were supported through the Hatch program of the National Institute of Food and Agriculture. This project has been funded in whole or in part with Federal funds from the National Institute of Allergy and Infectious Diseases (NIAID), NIH, Department of Health and Human Services, under Contract No. 75N93022C00036 from September 1, 2022. Seattle Structural Genomics Center for Infectious Disease was funded under NIAID Contracts No. HHSN272201700059C from September 1, 2017, through August 31, 2022; HHSN272201200025C from September 1, 2012, through August 31, 2017; and HHSN272200700057C from September 28, 2007, through September 27, 2012. The multiangle light scattering and small-angle X-ray scattering work was conducted at the ALS, a national user facility operated by Lawrence Berkeley National Laboratory on behalf of the U.S. Department of Energy (DOE), Office of Basic Energy Sciences, Office of Biological and Environmental Research, and Advanced Scientific Computing Research through the Integrated Diffraction Analysis Technologies program and the Biopreparedness Research Virtual Environment (BRaVE) Taskforce 5 (DOE-BRAVET5), under contract number DE-AC02-05CH11231. Additional support comes from the NIH project ALS-ENABLE (P30 GM124169) and a High-End Instrumentation Grant S10OD018483.

Author affiliations: [a]Seattle Structural Genomics Center for Infectious Disease, Seattle Children's Research Institute, Seattle, WA 98109; [b]Center for Global Infectious Disease Research, Seattle Children's Research Institute, Seattle, WA 98109; [c]Union Chimique Belge/Beryllium Discovery, Bainbridge Island, WA 98110; [d]Protein Structure and X-ray Crystallography Laboratory, The University of Kansas, Lawrence, KS 66047; [e]Chemistry Department, The University of Texas-Pan American, Edinburg, TX 78539; [f]New York Structural Biology Center, New York, NY 10027; [g]Department of Animal Sciences, Auburn University, Auburn, AL 36849; [h]Molecular Biophysics and Integrated Bioimaging, Lawrence Berkeley National Laboratory, Berkeley, CA 94720; [i]Department of Biomedical Information and Medical Education, University of Washington, Seattle, WA 98195; and [j]Department of Global Health, University of Washington, Seattle, WA 98195

1. S. Cusack, Eleven down and nine to go. *Nat. Struct. Biol.* **2**, 824–831 (1995).
2. M. A. Rubio Gomez, M. Ibba, Aminoacyl-tRNA synthetases. *RNA* **26**, 910–936 (2020).
3. M. B. Hoagland, E. B. Keller, P. C. Zamecnik, Enzymatic carboxyl activation of amino acids. *J. Biol. Chem.* **218**, 345–358 (1956).
4. P. Berg, E. J. Offengand, An enzymatic mechanism for linking amino acids to RNA. *Proc. Natl. Acad. Sci. U.S.A.* **44**, 78–86 (1958).
5. M. Sprinzl, F. Cramer, Accepting site for aminoacylation of $tRNA^{Phe}$ from yeast. *Nat. New Biol.* **245**, 3–5 (1973).
6. T. H. Fraser, A. Rich, Amino acids are not all initially attached to the same position on transfer RNA molecules. *Proc. Natl. Acad. Sci. U.S.A.* **72**, 3044–3048 (1975).
7. P. Berg, F. H. Bergmann, E. J. Ofengand, M. Dieckmann, The enzymic synthesis of amino acyl derivatives of ribonucleic acid I. The mechanism of leucyl-, valyl-, isoleucyl-, and methionyl ribonucleic acid formation. *J. Biol. Chem.* **236**, 1726–1734 (1961).
8. A. T. Norris, P. Berg, Mechanism of aminoacyl RNA synthesis: Studies with isolated aminoacyl adenylate complexes of isoleucyl RNA synthetase. *Proc. Natl. Acad. Sci. U.S.A.* **52**, 330–337 (1964).
9. E. W. Eldred, P. R. Schimmel, Rapid deacylation by isoleucyl transfer ribonucleic acid synthetase of isoleucine-specific transfer ribonucleic acid aminoacylated with valine. *J. Biol. Chem.* **247**, 2961–2963 (1972).
10. M. Yarus, Phenylalanyl-tRNA synthetase and isoleucyl-$tRNA^{Phe}$: A possible verification mechanism for aminoacyl-tRNA. *Proc. Natl. Acad. Sci. U.S.A.* **69**, 1915–1919 (1972).
11. A. R. Fersht, Editing mechanisms in protein synthesis. Rejection of valine by the isoleucyl-tRNA synthetase. *Biochemistry* **16**, 1025–1030 (1977).
12. H. Jakubowski, E. Goldman, Editing of errors in selection of amino acids for protein synthesis. *Microbiol. Rev.* **56**, 412–429 (1992).
13. M. J. Irwin, J. Nyborg, B. R. Reid, D. M. Blow, The crystal structure of tyrosyl-transfer RNA synthetase at 2.7 Å resolution. *J. Mol. Biol.* **105**, 577–586 (1976).

14. C. Zelwer, J. L. Risler, S. Brunie, Crystal structure of *Escherichia coli* methionyl-tRNA synthetase at 2.5 Å resolution. *J. Mol. Biol.* **155**, 63–81 (1982).
15. T. N. Bhat, D. M. Blow, P. Brick, J. Nyborg, Tyrosyl-tRNA synthetase forms a mononucleotide-binding fold. *J. Mol. Biol.* **158**, 699–709 (1982).
16. S. Cusack, C. Berthet-Colominas, M. Härtlein, N. Nassar, R. Leberman, A second class of synthetase structure revealed by X-ray analysis of *Escherichia coli* seryl-tRNA synthetase at 2.5 Å. *Nature* **347**, 249–255 (1990).
17. T. Webster, H. Tsai, M. Kula, G. A. Mackie, P. Schimmel, Specific sequence homology and three-dimensional structure of an aminoacyl transfer RNA synthetase. *Science* **226**, 1315–1317 (1984).
18. M. A. Rould, J. J. Perona, D. Söll, T. A. Steitz, Structure of *E. coli* glutaminyl-tRNA synthetase complexed with $tRNA^{Gln}$ and ATP at 2.8 Å resolution. *Science* **246**, 1135–1142 (1989).
19. G. Eriani, M. Delarue, O. Poch, J. Gangloff, D. Moras, Partition of tRNA synthetases into two classes based on mutually exclusive sets of sequence motifs. *Nature* **347**, 203–206 (1990).
20. J. Cavarelli *et al.*, The active site of yeast aspartyl-tRNA synthetase: Structural and functional aspects of the aminoacylation reaction. *EMBO J.* **13**, 327–337 (1994).
21. L. Ribas De Pouplana, P. Schimmel, Two classes of tRNA synthetases suggested by sterically compatible dockings on tRNA acceptor stem. *Cell* **104**, 191–193 (2001).
22. S. Cusack, M. Härtlein, R. Leberman, Sequence, structural and evolutionary relationships between class 2 aminoacyl-tRNA synthetases. *Nucleic Acids Res.* **19**, 3489–3498 (1991).
23. M. I. Valencia-Sánchez *et al.*, Structural insights into the polyphyletic origins of glycyl tRNA synthetases. *J. Biol. Chem.* **291**, 14430–14446 (2016).
24. J. J. Perona, I. Gruic-Sovulj, "Synthetic and editing mechanisms of aminoacyl-tRNA synthetases" in *Aminoacyl-tRNA Synthetases in Biology and Medicine*, S. Kim, Ed. (Springer, ed. 1, 2014), pp. 1–41.
25. D. L. Ostrem, P. Berg, Glycyl-tRNA synthetase: An oligomeric protein containing dissimilar subunits. *Proc. Natl. Acad. Sci. U.S.A.* **67**, 1967–1974 (1970).
26. F. Fasiolo, N. Befort, Y. Boulanger, J.-P. Ebel, Purification et quelques proprietes de la phenylalanyl-tRNA synthetase de levure de boulangerie. *Biochim. Biophys. Acta* **217**, 305–318 (1970).
27. L. Mosyak, L. Reshetnikova, Y. Goldgur, M. Delarue, M. G. Safro, Structure of phenylalanyl-tRNA synthetase from *Thermus thermophilus*. *Nat. Struct. Biol.* **2**, 537–547 (1995).
28. Y. Ju *et al.*, X-shaped structure of bacterial heterotetrameric tRNA synthetase suggests cryptic prokaryote functions and a rationale for synthetase classifications. *Nucleic Acids Res.* **49**, 10106–10119 (2021).
29. G. Eriani *et al.*, Role of dimerization in yeast aspartyl-tRNA synthetase and importance of the class II invariant proline. *Proc. Natl. Acad. Sci. U.S.A.* **90**, 10816–10820 (1993).
30. B. Kuhle, M. Hirschi, L. K. Doerfel, G. C. Lander, P. Schimmel, Structural basis for shape-selective recognition and aminoacylation of a D-armless human mitochondrial tRNA. *Nat. Commun.* **13**, 5100 (2022).
31. A. Yaremchuk, M. Tukalo, M. Grøtli, S. Cusack, A succession of substrate induced conformational changes ensures the amino acid specificity of *Thermus thermophilus* prolyl-tRNA synthetase: Comparison with histidyl-tRNA synthetase. *J. Mol. Biol.* **309**, 989–1002 (2001).
32. Q. Tian, C. Wang, Y. Liu, W. Xie, Structural basis for recognition of G-1-containing tRNA by histidyl-tRNA synthetase. *Nucleic Acids Res.* **43**, 2980–2990 (2015).
33. X. Qin *et al.*, Cocrystal structures of glycyl-tRNA synthetase in complex with tRNA suggest multiple conformational states in glycylation. *J. Biol. Chem.* **289**, 20359–20369 (2014).
34. R. Sankaranarayanan *et al.*, The structure of threonyl-tRNA synthetase-$tRNA^{Thr}$ complex enlightens its repressor activity and reveals an essential zinc ion in the active site. *Cell* **97**, 371–381 (1999).
35. M. Ruff *et al.*, Class II aminoacyl transfer RNA synthetases: Crystal structure of yeast aspartyl-trna synthetase complexed with $tRNA^{Asp}$. *Science* **252**, 1682–1689 (1991).
36. M. Naganuma *et al.*, The selective tRNA aminoacylation mechanism based on a single G•U pair. *Nature* **510**, 507–511 (2014).
37. Y. Goldgur *et al.*, The crystal structure of phenylalanyl-tRNA synthetase from *Thermus thermophilus* complexed with cognate $tRNA^{Phe}$. *Structure* **5**, 59–68 (1997).
38. Z. Yu *et al.*, Structural basis of a two-step tRNA recognition mechanism for plastid glycyl-tRNA synthetase. *Nucleic Acids Res.* **51**, 4000–4011 (2023).
39. L. Han *et al.*, The binding mode of orphan glycyl-tRNA synthetase with tRNA supports the synthetase classification and reveals large domain movements. *Sci. Adv.* **9**, eadf1027 (2023).
40. S. Doublié, G. Bricogne, C. Gilmore, C. W. Carter Jr., Tryptophanyl-tRNA synthetase crystal structure reveals an unexpected homology to tyrosyl-tRNA synthetase. *Structure* **3**, 17–31 (1995).
41. S. Sever, K. Rogers, M. J. Rogers, C. Carter Jr., D. Söll, *Escherichia coli* tryptophanyl-tRNA synthetase mutants selected for tryptophan auxotrophy implicate the dimer interface in optimizing amino acid binding. *Biochemistry* **35**, 32–40 (1996).
42. N. Shen, L. Guo, B. Yang, Y. Jin, J. Ding, Structure of human tryptophanyl-tRNA synthetase in complex with $tRNA^{Trp}$ reveals the molecular basis of tRNA recognition and specificity. *Nucleic Acids Res.* **34**, 3246–3258 (2006).
43. X.-L. Yang *et al.*, Two conformations of a crystalline human tRNA synthetase–tRNA complex: Implications for protein synthesis. *EMBO J.* **25**, 2919–2929 (2006).
44. A. Yaremchuk, I. Kriklivyi, M. Tukalo, S. Cusack, Class I tyrosyl-tRNA synthetase has a class II mode of cognate tRNA recognition. *EMBO J.* **21**, 3829–3840 (2002).
45. F. Dardel, G. Fayat, S. Blanquet, Molecular cloning and primary structure of the *Escherichia coli* methionyl-tRNA synthetase gene. *J. Bacteriol.* **160**, 1115–1122 (1984).
46. F. Fasiolo *et al.*, Cytoplasmic methionyl-tRNA synthetase from Bakers' yeast. A monomer with a post-translationally modified N terminus. *J. Biol. Chem.* **260**, 15571–15576 (1985).
47. Y. Motorin, J. P. Le Caer, J. P. Waller, Cysteinyl-tRNA synthetase from *Saccharomyces cerevisiae*. Purification, characterization and assignment to the genomic sequence YNL247w. *Biochimie* **79**, 731–740 (1997).
48. O. Nureki *et al.*, Architectures of class-defining and specific domains of glutamyl-tRNA synthetase. *Science* **267**, 1958–1965 (1995).
49. T. Terada *et al.*, Functional convergence of two lysyl-tRNA synthetases with unrelated topologies. *Nat. Struct. Biol.* **9**, 257–262 (2002).
50. O. Nureki *et al.*, Structure of an archaeal non-discriminating glutamyl-tRNA synthetase: A missing link in the evolution of Gln-$tRNA^{Gln}$ formation. *Nucleic Acids Res.* **38**, 7286–7297 (2010).
51. M. A. Rould, J. J. Perona, T. A. Steitz, Structural basis of anticodon loop recognition by glutaminyl-tRNA synthetase. *Nature* **352**, 213–218 (1991).
52. J. Lapointe, L. Duplain, M. Proulx, A single glutamyl-tRNA synthetase aminoacylates $tRNA^{Glu}$ and $tRNA^{Gln}$ in *Bacillus subtilis* and efficiently misacylates *Escherichia coli* $tRNA_1^{Gln}$ in vitro. *J. Bacteriol.* **165**, 88–93 (1986).
53. J. C. Salazar *et al.*, Coevolution of an aminoacyl-tRNA synthetase with its tRNA substrates. *Proc. Natl. Acad. Sci. U.S.A.* **100**, 13863–13868 (2003).
54. S. Skouloubris, L. R. De Pouplana, H. De Reuse, T. L. Hendrickson, A noncognate aminoacyl-tRNA synthetase that may resolve a missing link in protein evolution. *Proc. Natl. Acad. Sci. U.S.A.* **100**, 11297–11302 (2003).
55. S. Sekine, O. Nureki, A. Shimada, D. G. Vassylyev, S. Yokoyama, Structural basis for anticodon recognition by discriminating glutamyl-tRNA synthetase. *Nat. Struct. Biol.* **8**, 203–206 (2001).
56. J. C. Salazar, A. Ambrogelly, P. F. Crain, J. A. McCloskey, D. Söll, A truncated aminoacyl–tRNA synthetase modifies RNA. *Proc. Natl. Acad. Sci. U.S.A.* **101**, 7536–7541 (2004).
57. D. Y. Dubois *et al.*, An aminoacyl-tRNA synthetase-like protein encoded by the *Escherichia coli yadB* gene glutamylates specifically $tRNA^{Asp}$. *Proc. Natl. Acad. Sci. U.S.A.* **101**, 7530–7535 (2004).
58. S. Dasgupta, G. Basu, Evolutionary insights about bacterial GlxRS from whole genome analyses: Is GluRS2 a chimera? *BMC Evol. Biol.* **14**, 26 (2014).
59. S. Dasgupta *et al.*, Signatures of $tRNA^{Glx}$-specificity in proteobacterial glutamyl-tRNA synthetases. *Proteins Struct. Funct. Bioinforma.* **93**, 241–254 (2025).
60. Y. Hu, E. Guerrero, M. Keniry, J. Manrrique, J. M. Bullard, Identification of chemical compounds that inhibit the function of glutamyl-tRNA synthetase from *Pseudomonas aeruginosa*. *SLAS Discov.* **20**, 1160–1170 (2015).
61. E. F. Pettersen *et al.*, UCSF ChimeraX: Structure visualization for researchers, educators, and developers. *Protein Sci.* **30**, 70–82 (2021).
62. E. Krissinel, K. Henrick, Inference of macromolecular assemblies from crystalline state. *J. Mol. Biol.* **372**, 774–797 (2007).
63. R. Banerjee *et al.*, The zinc-binding site of a class I aminoacyl-tRNA synthetase is a SWIM domain that modulates amino acid binding via the tRNA acceptor arm. *Eur. J. Biochem.* **271**, 724–733 (2004).
64. J. Liu *et al.*, The zinc-binding site of *Escherichia coli* glutamyl-tRNA synthetase is located in the acceptor-binding domain. *J. Biol. Chem.* **270**, 15162–15169 (1995).
65. S. O. Moen *et al.*, Ligand co-crystallization of aminoacyl-tRNA synthetases from infectious disease organisms. *Sci. Rep.* **7**, 223 (2017).
66. N. Chongdar, S. Dasgupta, A. B. Datta, G. Basu, Dispensability of zinc and the putative zinc-binding domain in bacterial glutamyl-tRNA synthetase. *Biosci. Rep.* **35**, e00184 (2015).
67. S. Hayward, H. J. C. Berendsen, Systematic analysis of domain motions in proteins from conformational change: New results on citrate synthase and T4 lysozyme. *Proteins Struct. Funct. Genet.* **30**, 144–154 (1998).
68. L. Holm, C. Sander, Dali: A network tool for protein structure comparison. *Trends Biochem. Sci.* **20**, 478–480 (1995).
69. J. O. Schulze *et al.*, Crystal structure of a non-discriminating glutamyl-tRNA synthetase. *J. Mol. Biol.* **361**, 888–897 (2006).
70. T.-H. Ho *et al.*, Transcriptional expression of aminoacyl tRNA synthetase genes of *Xanthomonas oryzae* pv. *oryzae* (*Xoo*) on rice-leaf extract treatment and crystal structure of *Xoo* glutamyl-tRNA synthetase. *Crop Pasture Sci.* **68**, 434 (2017).
71. D. E. Davis *et al.*, Crystal structure of glutamyl-tRNA synthetase from *Helicobacter pylori*. *Acta Crystallogr. Sect. F Struct. Biol. Commun.* **80**, 335–340 (2024).
72. L. Brooks *et al.*, Crystal structures of glutamyl-tRNA synthetase from *Elizabethkingia anopheles* and *E. meningosepticum*. *Acta Crystallogr. Sect. F Struct. Biol. Commun.* **78**, 306–312 (2022).
73. S.-i. Sekine *et al.*, ATP binding by glutamyl-tRNA synthetase is switched to the productive mode by tRNA binding. *EMBO J.* **22**, 676–688 (2003).
74. S. C. Lovell, J. M. Word, J. S. Richardson, D. C. Richardson, The penultimate rotamer library. *Proteins Struct. Funct. Genet.* **40**, 389–408 (2000).
75. P.-M. Akochy, D. Bernard, P. H. Roy, J. Lapointe, Direct glutaminyl-tRNA biosynthesis and indirect asparaginyl-tRNA biosynthesis in *Pseudomonas aeruginosa* PAO1. *J. Bacteriol.* **186**, 767–776 (2004).
76. M. Ibba *et al.*, Substrate recognition by class I lysyl-tRNA synthetases: A molecular basis for gene displacement. *Proc. Natl. Acad. Sci. U.S.A.* **96**, 418–423 (1999).
77. J. Lapointe, D. Söll, Glutamyl transfer ribonucleic acid synthetase of *Escherichia coli*. *J. Biol. Chem.* **247**, 4966–4974 (1972).
78. S. K. Mitra, A. H. Mehler, The arginyl transfer ribonucleic acid synthetase of *Escherichia coli*. *J. Biol. Chem.* **242**, 5490–5494 (1967).
79. J. M. Ravel, S.-F. Wang, C. Heinemeyer, W. Shive, Glutamyl and glutaminyl ribonucleic acid synthetases of *Escherichia coli* W. *J. Biol. Chem.* **240**, 432–438 (1965).
80. A. Shimada, O. Nureki, M. Goto, S. Takahashi, S. Yokoyama, Structural and mutational studies of the recognition of the arginine tRNA-specific major identity element, A20, by arginyl-tRNA synthetase. *Proc. Natl. Acad. Sci. U.S.A.* **98**, 13537–13542 (2001).
81. P. P. Chan, T. M. Lowe, GtRNAdb 2.0: An expanded database of transfer RNA genes identified in complete and draft genomes. *Nucleic Acids Res.* **44**, D184–D189 (2016).
82. N. Krahn, J. T. Fischer, D. Söll, Naturally occurring tRNAs with non-canonical structures. *Front. Microbiol.* **11**, 596914 (2020).
83. S. Sekine *et al.*, Structural bases of transfer RNA-dependent amino acid recognition and activation by glutamyl-tRNA synthetase. *Structure* **14**, 1791–1799 (2006).
84. Y. Nakamura *et al.*, Complete genome structure of *Gloeobacter violaceus* PCC 7421, a cyanobacterium that lacks thylakoids. *DNA Res.* **10**, 137–145 (2003).
85. M. Francin, M. Kaminska, P. Kerjan, M. Mirande, The N-terminal domain of mammalian lysyl-tRNA synthetase is a functional tRNA-binding domain. *J. Biol. Chem.* **277**, 1762–1769 (2002).
86. M. Frugier, L. Moulinier, R. Giegé, A domain in the N-terminal extension of class IIb eukaryotic aminoacyl-tRNA synthetases is important for tRNA binding. *EMBO J.* **19**, 2371–2380 (2000).
87. Y. Escamilla *et al.*, Glutaminyl-tRNA synthetase from *Pseudomonas aeruginosa*: Characterization, structure, and development as a screening platform. *Protein Sci.* **29**, 905–918 (2020).
88. P. Myler *et al.*, The Seattle Structural Genomics Center for Infectious Disease (SSGCID). *Infect. Disord. Drug Targets* **9**, 493–506 (2009).
89. N. Pena, D. M. Dranow, Y. Hu, Y. Escamilla, J. M. Bullard, Characterization and structure determination of prolyl-tRNA synthetase from *Pseudomonas aeruginosa* and development as a screening platform. *Protein Sci.* **28**, 727–737 (2019).
90. S. A. Lee *et al.*, General and condition-specific essential functions of *Pseudomonas aeruginosa*. *Proc. Natl. Acad. Sci. U.S.A.* **112**, 5189–5194 (2015).
91. B. E. Poulsen *et al.*, Defining the core essential genome of *Pseudomonas aeruginosa*. *Proc. Natl. Acad. Sci. U.S.A.* **116**, 10072–10080 (2019).
92. C. M. Bryan *et al.*, High-throughput protein production and purification at the Seattle Structural Genomics Center for Infectious Disease. *Acta Crystallograph. Sect. F Struct. Biol. Cryst. Commun.* **67**, 1010–1014 (2011).

93. R. Choi *et al.*, Immobilized metal–affinity chromatography protein–recovery screening is predictive of crystallographic structure success. *Acta Crystallograph. Sect. F Struct. Biol. Cryst. Commun.* **67**, 998–1005 (2011).
94. C. Aslanidis, P. J. De Jong, Ligation-independent cloning of PCR products (LIC-PCR). *Nucleic Acids Res.* **18**, 6069–6074 (1990).
95. P. Savitsky *et al.*, High-throughput production of human proteins for crystallization: The SGC experience. *J. Struct. Biol.* **172**, 3–13 (2010).
96. F. W. Studier, Protein production by auto-induction in high-density shaking cultures. *Protein Expr. Purif.* **41**, 207–234 (2005).
97. D. J. Rosenberg, G. L. Hura, M. Hammel, "Size exclusion chromatography coupled small angle X-ray scattering with tandem multiangle light scattering at the SIBYLS beamline" in *Methods in Enzymology*, J. A. Tainer, Ed. (Elsevier, 2022), pp. 191–219.
98. J. B. Hopkins, *BioXTAS RAW 2:* New developments for a free open-source program for small-angle scattering data reduction and analysis. *J. Appl. Crystallogr.* **57**, 194–208 (2024).
99. B. Webb, A. Sali, Comparative protein structure modeling using MODELLER. *Curr. Protoc. Bioinformatics* **54**, 5.6.1–5.6.37 (2016).
100. D. Schneidman-Duhovny, M. Hammel, J. A. Tainer, A. Sali, Accurate SAXS profile computation and its assessment by contrast variation experiments. *Biophys. J.* **105**, 962–974 (2013).
101. T. D. Grant, *Ab initio* electron density determination directly from solution scattering data. *Nat. Methods* **15**, 191–193 (2018).
102. R. P. Rambo, J. A. Tainer, Accurate assessment of mass, models and resolution by small-angle scattering. *Nature* **496**, 477–481 (2013).
103. N. R. Hajizadeh, D. Franke, C. M. Jeffries, D. I. Svergun, Consensus Bayesian assessment of protein molecular mass from solution X-ray scattering data. *Sci. Rep.* **8**, 7204 (2018).
104. J. H. Pereira, R. P. McAndrew, G. P. Tomaleri, P. D. Adams, Berkeley Screen: A set of 96 solutions for general macromolecular crystallization. *J. Appl. Crystallogr.* **50**, 1352–1358 (2017).
105. W. Kabsch, *XDS*. *Acta Crystallogr. D Biol. Crystallogr.* **66**, 125–132 (2010).
106. C. Vonrhein *et al.*, Data processing and analysis with the *autoPROC* toolbox. *Acta Crystallogr. D Biol. Crystallogr.* **67**, 293–302 (2011).
107. A. J. McCoy *et al.*, *Phaser* crystallographic software. *J. Appl. Crystallogr.* **40**, 658–674 (2007).
108. P. Emsley, B. Lohkamp, W. G. Scott, K. Cowtan, Features and development of *Coot*. *Acta Crystallogr. D Biol. Crystallogr.* **66**, 486–501 (2010).
109. D. Liebschner *et al.*, Macromolecular structure determination using X-rays, neutrons and electrons: Recent developments in *Phenix*. *Acta Crystallogr. Sect. D Struct. Biol.* **75**, 861–877 (2019).
110. C. J. Williams *et al.*, MolProbity: More and better reference data for improved all-atom structure validation. *Protein Sci.* **27**, 293–315 (2018).
111. E. F. Pettersen *et al.*, UCSF Chimera–A visualization system for exploratory research and analysis. *J. Comput. Chem.* **25**, 1605–1612 (2004).
112. E. C. Meng, E. F. Pettersen, G. S. Couch, C. C. Huang, T. E. Ferrin, Tools for integrated sequence-structure analysis with UCSF Chimera. *BMC Bioinformatics* **7**, 339 (2006).
113. A. Waterhouse *et al.*, SWISS-MODEL: Homology modelling of protein structures and complexes. *Nucleic Acids Res.* **46**, W296–W303 (2018).
114. R. C. Edgar, MUSCLE: Multiple sequence alignment with high accuracy and high throughput. *Nucleic Acids Res.* **32**, 1792–1797 (2004).
115. X. Robert, P. Gouet, Deciphering key features in protein structures with the new ENDscript server. *Nucleic Acids Res.* **42**, W320–W324 (2014).
116. M. Szymanski, Aminoacyl-tRNA synthetases database Y2K. *Nucleic Acids Res.* **28**, 326–328 (2000).
117. R. C. Edgar, Search and clustering orders of magnitude faster than BLAST. *Bioinformatics* **26**, 2460–2461 (2010).
118. I. Letunic, P. Bork, Interactive Tree Of Life (iTOL): An online tool for phylogenetic tree display and annotation. *Bioinformatics* **23**, 127–128 (2007).
119. S. J. Mayclin, D. M. Dranow, D. D. Lorimer, T. E. Edwards, Crystal structure of glutamyl-tRNA synthetase GluRS from P*seudomonas aeruginosa*. Protein Data Bank. https://www.rcsb.org/structure/5TGT. Deposited 28 September 2016.
120. S. Seibold, S. Lovell, K. P. Battaile, M. K. Fenwick, Crystal structure of glutamyl-tRNA synthetase GluRS from *Pseudomonas aeruginosa* (Zinc bound). Protein Data Bank. https://www.rcsb.org/structure/8VC5. Deposited 13 December 2023.
121. M. K. Fenwick *et al.*, SEC-MALS-SAXS studies of *Pseudomonas aeruginosa* GluRS. Simple Scattering. https://simplescattering.com/open_dataset/xsbhevph. Deposited 17 November 2023.